



Aerodynamic and dynamic analyses of three common 4.5 mm-caliber pellets in a transonic flow

M. Rafeie and A.R. Teymourtash*

Department of Mechanical Engineering, Ferdowsi University of Mashhad, Mashhad, Iran.

Received 26 November 2014; received in revised form 8 February 2015; accepted 24 May 2016

KEYWORDS

Navier-stokes equations;
 Jameson method;
 Transonic flow;
 Dynamic analysis;
 Air gun pellet.

Abstract. In this paper, a numerical solution of the Navier-Stokes equations is considered using the Jameson method in the transonic flow regime over three air gun pellets. The considered pellets have the same caliber of 4.5 mm, but different nose shapes; they are axisymmetric projectiles of three basic types, namely wadcutter, sharp pointed, and round-nose. After these pellets have been modeled geometrically, the Navier-Stokes equations as the governing equations of the flow field around the pellets are solved. Computed aerodynamic results have been used in order to analyze the trajectories of the projectiles, dynamically. The variation of the drag coefficient by Mach number of the free stream flow, which is a key point for the dynamic analysis of the projectile motion, has been obtained. The dynamic analysis of the motion of pellets precisely describes the trajectory and how the velocity of the pellet and the altitude slump with time and location. Relying on these analyses, from both aerodynamic and dynamic points of view, the round-nose pellet in a variable range of Mach numbers shows the best aerodynamic and dynamic behaviors in comparison with other pellets.

© 2016 Sharif University of Technology. All rights reserved.

1. Introduction

One of the most practical topics in aerodynamics is the analysis of the motion of a projectile, which entails calculating a variety of aerodynamic and dynamic parameters. Having analyzed a reacting M864-base bleed projectile using Navier-Stokes computations in 1995, Nietubicz and Gibeling investigated the impact of the thrust force on velocity vectors in the wake area at Mach numbers of less than 1 to about 3, and eventually predicted the missile trajectory accurately [1]. Siltan used Navier-Stokes computations for a spinning projectile from subsonic to supersonic speeds in different angles of attack in order to anticipate the influence of whirling on the fluid flow [2]. Sahu blended

the Computational Fluid Dynamics (CFD) with Rigid Body Dynamics (RBD) and could successfully simulate the trajectory of several projectiles and missiles with and without rotational movements in unsteady conditions [3]. Weinacht, who had already solved the Navier-Stokes for predictions of pitch damping of axisymmetric projectiles [4], cooperated with Siltonin to show the effect of rifling grooves on the performance of small-caliber ammunition [5]. They further cooperated with De Spirito in a numerical-experimental work using a wind tunnel, which resulted in explaining how forces and momentums due to the spinning of the projectile affect its dynamic stability [6]. Some years later, Sahu described a computational study undertaken to compute the unsteady free flight aerodynamics of a spinning projectile across the speed regime from subsonic to supersonic speeds using an advanced coupled CFD/RBD technique. The CFD part of his work used an unstructured time-accurate Navier-Stokes computational technique. The coupled CFD/RBD method

*. Corresponding author. Tel.: +98 51 38805030;
 Fax: +98 51 38763304
 E-mail addresses: mehdi.rafeie@gmail.com (M. Rafeie);
 teymourtash@um.ac.ir (A.R. Teymourtash)

allowed time-accurate virtual fly-out simulations of projectiles and simultaneously predicted the aerodynamics and flight dynamics in an integrated manner [7]. Then, Sahu and Heavey used both steady-state CFD and coupled CFD/RBD techniques to compute the aerodynamics associated with the free flight of the finned projectile both with and without the micro flaps. Navier-Stokes computations were performed and steady-state solutions were obtained from subsonic to supersonic speeds. Computed results of their work showed that the micro flaps were ineffective at transonic speeds and effective at supersonic velocities [8]. Amitesh Kumar et al. numerically studied the flow around a conical nose with rounded tail projectile for subsonic, transonic, and supersonic flow regimes. It was observed that rounded tail was a better option than boat tail so far as drag force was concerned [9].

In this paper, the aerodynamic and dynamic analysis of the three common projectiles of air guns, which have not been reported before, has been carried out numerically. The considered projectiles are of basic types, namely a wadcutter, a sharp pointed, and a round-nose pellet, respectively. To achieve this point, after geometrically simulating the pellets, the Navier-Stokes equations as the governing equations of the flow field around the pellets were solved. The effect of geometry of the pellets on parameters such as drag and pressure was investigated. Furthermore, the obtained results were used in the numerical solution of a system of ordinary differential equations as the governing dynamic equations of the motion of projectile. In this way, the trajectory and the velocity of the pellets were predicted.

2. Simulating the geometry of pellets

The first step of the analysis is to simulate the geometry of the pellets. Here, the simulation process has been

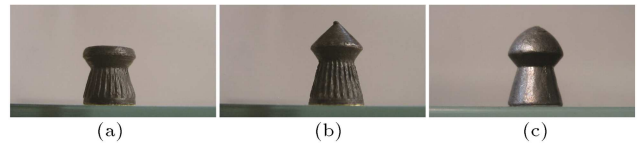


Figure 1. The considered 4.5 mm-caliber: (a) Wadcutter; (b) sharp pointed; and (c) round-nose.

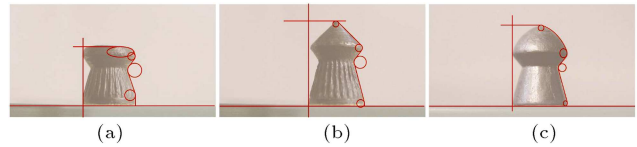


Figure 2. Fitting curves to the geometry of the (a) 1st pellet, (b) 2nd pellet, and (c) 3rd pellet.




carried out with the aid of a digital camera. Some precise photographs have been taken using the super-macro photographic mode of the camera in a bright environment in order to increase the quality of the taken photos (Figure 1). Afterwards, the geometry of the pellets has been precisely fitted with some lines and curves, which is indicated in Figure 2. Next, all required coordinates specifying the pellet geometries have been extracted with the aid of a digitizer software application. Finally, the dimensions of the pellets have been measured by a caliper with ± 0.01 mm of resolution and the pellets have been weighed by a digital weighing scale with an accuracy of ± 0.1 g to find out the density of the pellets (Table 1). The resulting plot of the pellets is depicted in Figure 3.

3. Meshing of the solution domain

One of the most common methods of grid generation is the elliptic method. In this method, both physical boundary of the pellet body and an outer boundary including the pellet should be defined.

The outer boundary specifies the region in which

Table 1. The physical measurements of the pellets.

Schematic	Pellet	Name	Length (mm)	Caliber (mm)	Mass (g)
	1st pellet	Wadcutter	5.00	4.50	0.5
	2nd pellet	Sharp pointed	7.00	4.50	0.6
	3rd pellet	Round-nose	6.50	4.50	0.5

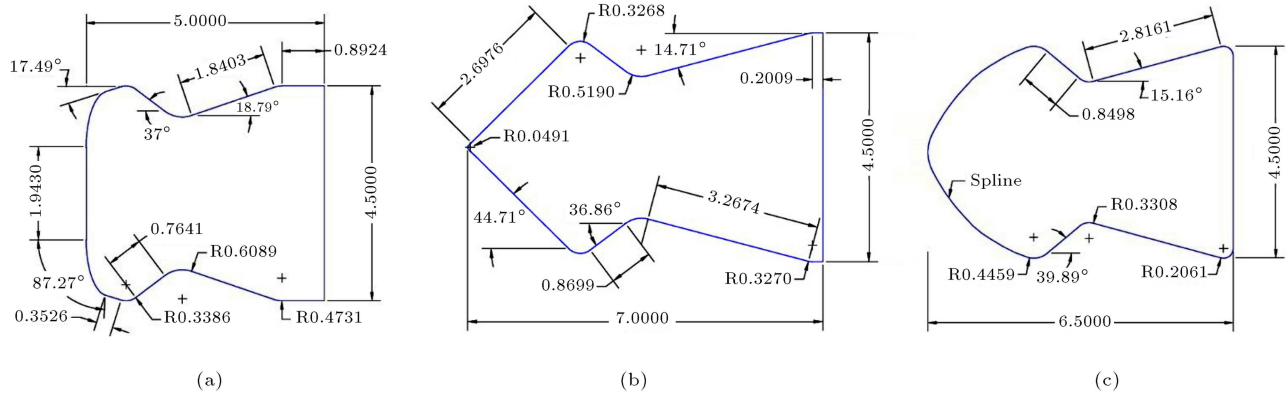


Figure 3. The plot of the (a) 1st pellet, (b) 2nd pellet, and (c) 3rd pellet.

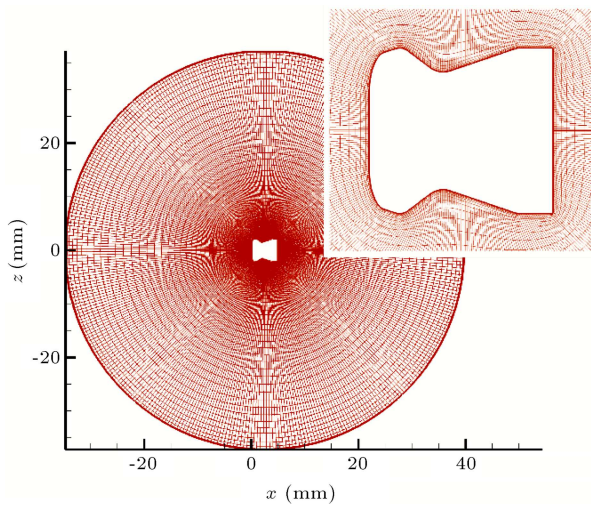


Figure 4. Meshing of the solution domain.

the fluid flow should be solved. This domain, as shown here, is defined as a circular area around the body with a radius 15 times larger than an imaginary radius of the projectile including 377 by 60 grid points. Since the fluid flow is viscous, the cells which are close to the body have been more compressed to capture the boundary layer effect precisely. The generated grid in the solution domain for the first pellet is shown in Figure 4.

4. Governing aerodynamic equations

In order to analyze the pellets aerodynamically, two-dimensional axisymmetric compressible Navier-Stokes equations have been numerically solved in a cylindrical coordinate system (x, r, θ) using the explicit Jameson method. This scheme uses central differencing which is formally of second-order accuracy in space [10-12]. The governing equations of the fluid flow can be written as:

$$\frac{\partial W}{\partial t} + \frac{\partial E_i}{\partial x} + \frac{\partial F_i}{\partial r} + H_i = \frac{\partial E_v}{\partial x} + \frac{\partial F_v}{\partial r} + H_v, \quad (1)$$

W is a dependent variables; E_i and F_i are convective

flux vectors, and H_i is an inviscid source term; they are defined as:

$$W = \begin{bmatrix} \rho \\ \rho u \\ \rho v \\ \rho e \end{bmatrix}, \quad (2)$$

$$E_i = \begin{bmatrix} \rho u \\ \rho u^2 + P \\ \rho uv \\ u(\rho e + P) \end{bmatrix}, \quad (3)$$

$$F_i = \begin{bmatrix} \rho v \\ \rho uv \\ \rho v^2 + P \\ v(\rho e + P) \end{bmatrix}, \quad (4)$$

$$H_i = \begin{bmatrix} 0 \\ 0 \\ P \\ - \\ r \\ 0 \end{bmatrix}. \quad (5)$$

In addition, E_v and F_v are viscous flux vectors, and H_v is a viscous source term, which are obtained as follows:

$$E_v = \begin{bmatrix} 0 \\ \tau_{xx} \\ \tau_{xr} \\ u\tau_{xx} + v\tau_{xr} - q_x \end{bmatrix}, \quad (6)$$

$$F_v = \begin{bmatrix} 0 \\ \tau_{rx} \\ \tau_{rr} \\ u\tau_{rx} + v\tau_{rr} - q_r \end{bmatrix}, \quad (7)$$

$$H_v = \begin{bmatrix} 0 \\ 0 \\ \tau_{rr} - \tau_{\theta\theta} \\ r \\ 0 \end{bmatrix}, \quad (8)$$

where ρ and P are the local dimensionless density and pressure, respectively. τ_{xx} , τ_{rr} , and $\tau_{\theta\theta}$ are normal stresses; τ_{xr} and τ_{rx} are shear stresses; and e is the summation of internal and kinetic energy for the mass unit of fluid which can be obtained from the following expression:

$$e = \frac{P}{\rho(\gamma - 1)} + \frac{1}{2}(u^2 + v^2), \tag{9}$$

where $\gamma = C_p/C_v$. Here, the terms C_p and C_v are the specific heat constants for constant pressure and constant volume processes, respectively. Besides, the dimensionless normal and shear stresses are:

$$\tau_{xx} = \frac{2}{3} \frac{\mu}{Re_\infty} \left(2 \frac{\partial u}{\partial x} - \frac{\partial v}{\partial r} - \frac{v}{r} \right), \tag{10}$$

$$\tau_{rr} = \frac{2}{3} \frac{\mu}{Re_\infty} \left(2 \frac{\partial v}{\partial r} - \frac{\partial u}{\partial x} + \frac{v}{r} \right), \tag{11}$$

$$\tau_{\theta\theta} = \frac{2}{3} \frac{\mu}{Re_\infty} \left(\frac{\partial u}{\partial x} + \frac{\partial v}{\partial r} - 2 \frac{v}{r} \right), \tag{12}$$

$$\tau_{xr} = \tau_{rx} = \frac{\mu}{Re_\infty} \left(\frac{\partial u}{\partial r} + \frac{\partial v}{\partial x} \right), \tag{13}$$

where Re_∞ is Reynolds number of the free-stream flow defined as follows:

$$Re_\infty = \frac{\rho(M_\infty C)D}{\mu}, \tag{14}$$

where M_∞ is the Mach number of free stream flow, C is the speed of sound, and D is the diameter of the pellet which equals its caliber. μ is the dynamic viscosity of ambient air, which with the assumption of the ideal gas for surrounding air may be evaluated using the Sutherland’s formula [13]. Moreover, the dimensionless heat fluxes in Eqs. (4)-(6) and (4)-(7) are described as:

$$q_x = -\frac{\mu}{Re_\infty(\gamma - 1)M_\infty^2 Pr} \frac{\partial T}{\partial x}, \tag{15}$$

$$q_y = -\frac{\mu}{Re_\infty(\gamma - 1)M_\infty^2 Pr} \frac{\partial T}{\partial r}, \tag{16}$$

where Pr is the Prandtl number and T is the local dimensionless temperature. The parameter T can be expressed as:

$$T = \gamma M_\infty^2 \frac{P}{\rho}. \tag{17}$$

The governing unsteady aerodynamic equations are always hyperbolic regardless of the flow regime. Therefore, the Jameson’s time-marching technique has been applied to the computations in order to achieve steady-state solution for each flight Mach number as the input

boundary condition; beginning with guessed initial flow distributions, the unsteady equations are integrated in time until the solution becomes independent of time and can be taken as the steady-state solution. Consequently, the average rate of global change of density residual throughout the calculation domain is used as the convergence criterion of the numerical solution. This is a commonly used criterion in computational fluid dynamics and is defined as:

$$R_{\text{error}} = \frac{1}{N_{\text{node}} \Delta t} \left[\sqrt{\sum_{ij} (\delta \rho_{ij}^2)} \right], \tag{18}$$

where N_{node} is the total number of nodes, and $\delta \rho$ is the change in density in two successive steps. The calculation can be regarded as converged when $R_{\text{error}} < 0.01\%$ [10,14,15]. The time spent for solving the Navier-Stokes equations for a specific Mach number is about five minutes using an Intel® Core™ 2 Duo CPU 2.53 GHz.

5. Governing dynamic equations

The governing dynamic equations have been considered for the purpose of obtaining the trajectory of the pellets. These equations are derived using Newton’s second law of motion along the normal and tangent directions of the trajectory path. The kinetic diagram of the pellet motion is shown in Figure 5.

The position vector of the projectile can be written as:

$$\vec{r} = x\hat{i} + z\hat{k}, \tag{19}$$

where x and z are the horizontal and vertical components of the position vector, respectively. Also, \hat{i} and \hat{k} are unit vectors along x and z directions in of the given order. Two consecutive derivatives of \vec{r} give velocity and acceleration vectors as:

$$\vec{v} = \dot{\vec{r}} = \dot{x}\hat{i} + \dot{z}\hat{k}, \tag{20}$$

$$\vec{a} = \ddot{\vec{r}} = \ddot{x}\hat{i} + \ddot{z}\hat{k}. \tag{21}$$

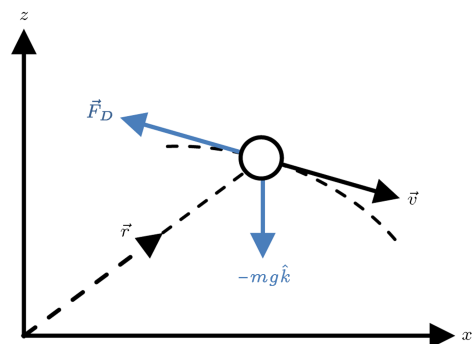


Figure 5. The kinetic diagram of the projectile’s motion.

Besides, the drag force \vec{F}_D is proportional to the projectile velocity, but opposite to the direction of motion. Therefore, it can be expressed as:

$$\vec{F}_D = - \left(\frac{1}{2} C_D \rho_\infty v^2 A_P \right) \hat{e}_t, \quad (22)$$

where C_D is the drag coefficient, ρ_∞ is the density of free stream flow, v is the magnitude of velocity vector \vec{v} , A_P is the platform area of the projectile, and $\hat{e}_t = \vec{v}/|\vec{v}|$ is the tangential unit vector. Applying Newton's second law gives:

$$-mg\hat{k} - \frac{C_D \rho_\infty v^2 A_P}{2} \left(\frac{\dot{x}\hat{i} + \dot{z}\hat{k}}{\sqrt{\dot{x}^2 + \dot{z}^2}} \right) = m \left(\ddot{x}\hat{i} + \ddot{z}\hat{k} \right). \quad (23)$$

Thus:

$$\begin{cases} m\ddot{x} = -\frac{C_D \rho_\infty A_P}{2} \dot{x}^2 \sqrt{1 + (\dot{z}/\dot{x})^2} \\ m\ddot{z} = -mg - \frac{C_D \rho_\infty A_P}{2} \dot{x}\dot{z} \sqrt{1 + (\dot{z}/\dot{x})^2}, \end{cases} \quad (24)$$

where m is the projectile mass and g is the gravitational acceleration. The term $(\dot{z}/\dot{x})^2$ has an infinitesimal value and hence is negligible. The following initial conditions are assumed for the above system of differential equations:

$$\begin{cases} \dot{x}(0) = v_0 \\ \dot{z}(0) = 0 \\ x(0) = 0 \\ z(0) = 0 \end{cases} \quad (25)$$

where v_0 is the initial velocity of the air gun pellet.

In this paper, the system of differential equations (Eqs. (5) and (6)) has been solved using fourth-order Runge-Kutta method [16]. As is evident, the system of equations involves the drag coefficient C_D which itself is a function of Mach number. A table of C_D versus M_∞ values has been provided by solving the governing aerodynamic equations at various Mach numbers. Thus, the dynamic analysis of the pellet motion at each time-step essentially depends on the aerodynamic results; however, since the drag coefficient $C_D = C_D(M_\infty)$ is not available as an explicit function, utilizing an interpolation method, like linear regression, between the available C_D values from the above mentioned $C_D - M_\infty$ table is inevitable.

6. The validation of numerical solution

Before proceeding further, the numerical solution should be validated. Therefore, the fluid flow over a particular projectile has been solved using the Jameson method and the obtained results have been compared

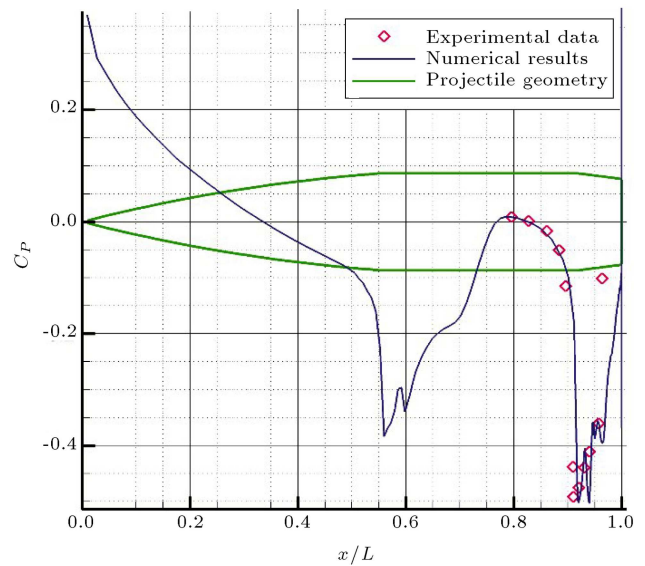


Figure 6. The validation of the numerical solution.

with both the numerical results of Pasandideh Fard and Srinivas [17] and the experimental data reported by Lin and Chieng [18]. Comparison of results is illustrated in Figure 6. As can be clearly seen, there is a proper agreement between the numerical solution and the experimental data.

7. Aerodynamic results and discussions

In this section, the numerical solution of the Navier-Stokes equations is elaborated, which includes the analysis of the streamlines, the drag and pressure coefficients together with the Mach and pressure contours.

The streamlines of the flow field over all pellets at different Mach numbers ($M < 1, M = 1, M > 1$) are shown in Figure 7. The wake area, which is generated in the downstream right behind the pellets, is a low-pressure region. Since at a particular Mach number, the wake area of the first, second, and third pellets becomes smaller, these projectiles are respectively subjected to a smaller pressure drag force during their flight in a transonic flow. On the other hand, as can be inferred from the figure, the wake area of a certain pellet decreases with increase in Mach number; however, investigating fluid flow parameters reveals that the more the Mach numbers are, the less the pressure values are in the wake area. Hence, the pressure drag force increases as Mach number rises, because the flow field experiences more pressure differences between the upstream and downstream at higher Mach numbers.

The drag coefficient C_D versus Mach number is shown in Figure 8. Inasmuch as the acting drag force on the pellet is defined as product of dynamic pressure and the drag coefficient, the C_D diagram confirms what was

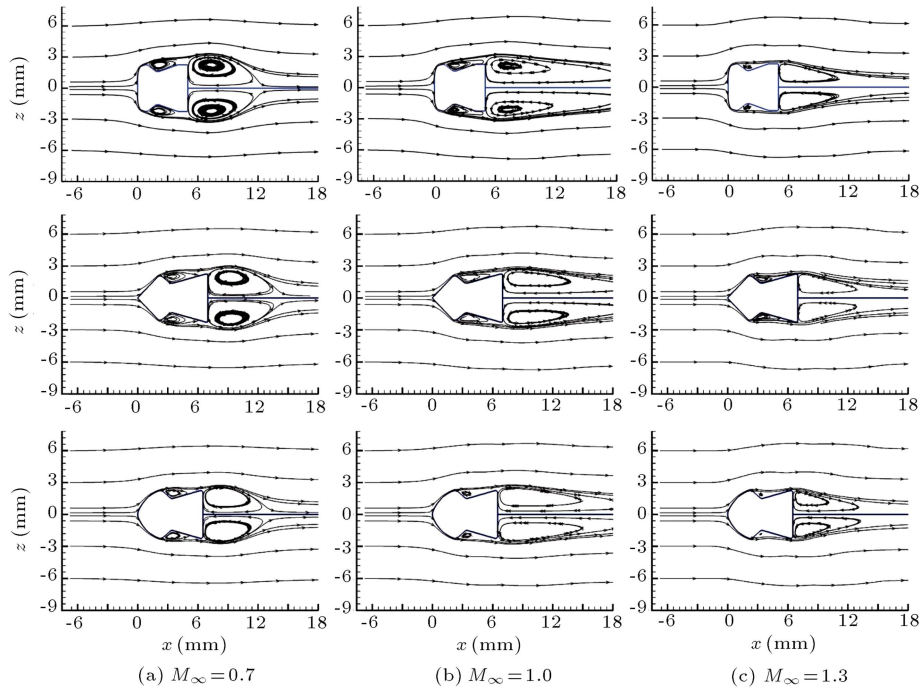


Figure 7. The streamlines at (a) $M_\infty = 0.7$, (b) $M_\infty = 1.0$, and (c) $M_\infty = 1.3$.

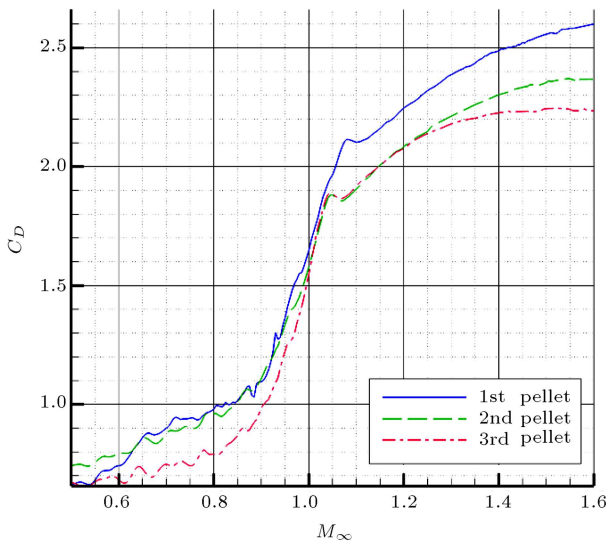


Figure 8. The drag coefficient C_D versus Mach number.

already concluded from the analysis of the reduction effect of the wake area on the pellets.

The pressure coefficient is defined as:

$$C_P = \frac{P - P_\infty}{\rho_\infty (M_\infty C)^2 A_P / 2}, \tag{26}$$

where P and P_∞ are local and atmospheric pressure, respectively. Also, ρ_∞ is the density of free stream flow and C is the speed of sound. The diagram of pressure coefficient C_P at different Mach numbers is shown in Figure 9. Since the dynamic pressure for all pellets remains constant at a certain Mach number,

any changes in the C_P diagram would be due to the variation of the static pressure. Thus, the sudden slump of the C_P at the front side of the first pellet in comparison with those of the other ones indicates a significant difference between P and P_∞ in this area, which signifies that the streamlines become close together and cause a speed growth from the front stagnation point to a maximum value at the edges. Again, such a steep gradient verifies that the first pellet is faced with a situation at which the acting pressure drag is more than those of the others. As a result, a steep slope in front of a projectile causes noticeable pressure drag.

Furthermore, C_P has a positive value up to the front stagnation point, where P is greater than P_∞ , causing the fluid flow to stagnate at this region. In contrast, the pressure gradient is reversed after the stagnation point and the flow velocity increases up to the minimum point of the C_P diagram, where the flow experiences its maximum velocity. This can also be seen in Figure 10, indicating Mach number contours at $M_\infty = 0.7$ around the first pellet. At this Mach number, the minimum point of the C_P diagram occurs just before $x = 0.4$ mm, which is coincident with the maximum velocity of the fluid flow as depicted in the figure. In addition, Figure 7 illustrates the variation of the flow velocity too. As can be noticed, the distance between streamlines is considerably reduced just after the stagnation point, which proves the previous analyses. Many number contours around the pellets at $M_\infty = 1.0$ are shown in Figure 11 to clarify more this issue.

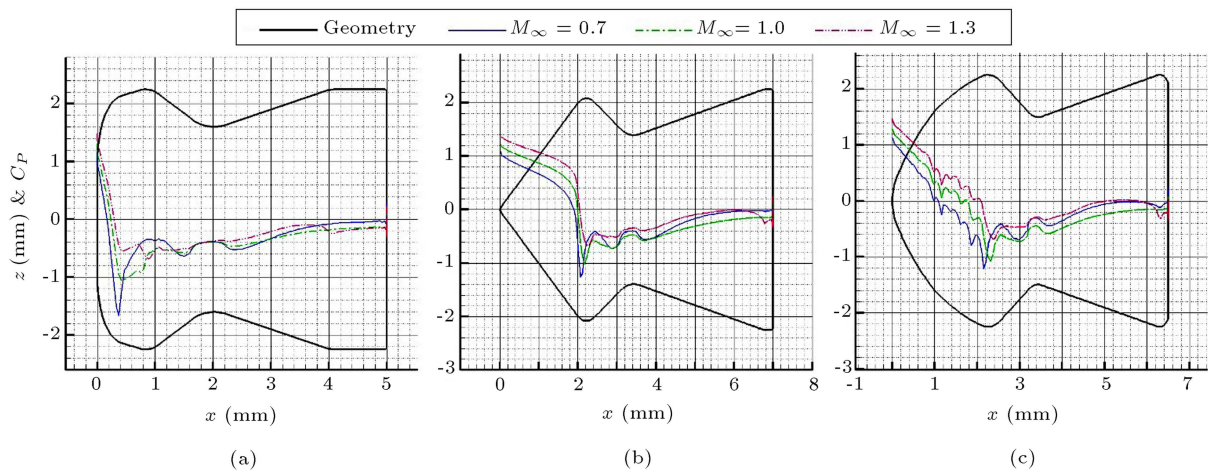


Figure 9. Pressure coefficients at $M_\infty=0.7, 1.0, 1.3$ for the (a) 1st pellet, (b) 2nd pellet, and (c) 3rd pellet.

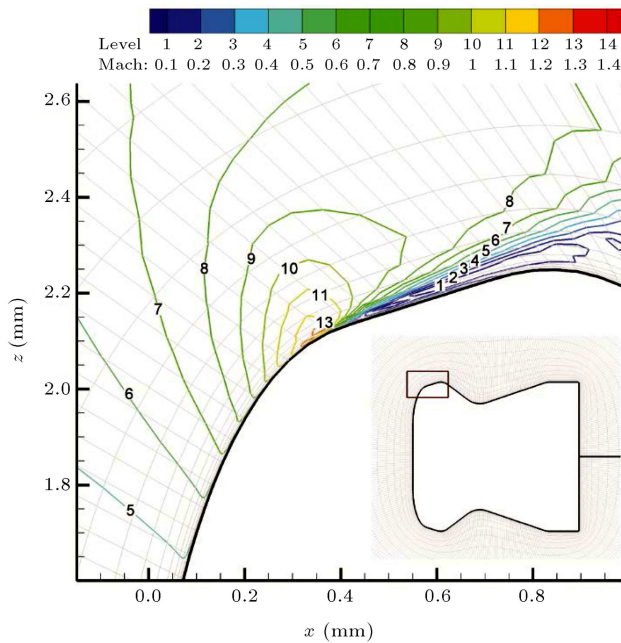


Figure 10. The Mach number contours around the maximum velocity point at $M_\infty = 0.7$.

Finally, the pressure contours shown in Figure 12 are considered. The wake area, as a low-pressure region located behind the pellet, can be distinctly identified. As is evident, the minimum pressure contour level occurs around the maximum velocity point.

8. Dynamic results and discussions

In this section, the solution of the system of differential equations (Eqs. (5) and (6)) as the governing equations of the motion of pellets, is considered for the first 25 meters of their path in order to examine the trajectory, Mach reduction, momentum changes, and the time at which the projectile travels a specific distance.

The trajectories of the first pellet at various initial Mach numbers (M_0) are shown in Figure 13. As

is expected, the deviation of the trajectory from a horizontal line decreases with increase in M_0 . Here, the altitude change is considered at three initial Mach numbers of 0.7, 1.0, and 1.3 to cover the whole range of the transonic flow. The altitude change amount at $M_0 = 1.0$ is taken as a reference value. As can be seen, the difference between the reference value and that of $M_0 = 0.7$ is more than the difference in case of $M_0 = 1.3$, which suggests that the altitude change would be more salient at lower initial Mach numbers.

In addition, the velocity loss of the first pellet at various initial Mach numbers in the first 25 meters of trajectory is shown in Figure 14. As this diagram illustrates, the distance is traveled faster at higher initial Mach numbers. It is worthy of note that the difference between initial and final velocities of the pellet is quite more than those of the lower initial Mach numbers. Obviously, this result is consequential where the final momentum of the pellet is the point that we are interested in.

The Mach reduction of all pellets during the first 25 m of their path is depicted in Figure 15. Although the C_D diagram of the pellets indicates that the third pellet has the minimum amount of the drag coefficient, Figure 15 reveals that the minimum value of Mach number reduction belongs to the second pellet. This apparent contradiction is resolved by taking the mass of the pellets into account. As it is shown in Table 1, the second pellet is heavier than the other ones. Obviously, to give the same initial velocity to two projectiles having different weights, the heavier one needs more momentum. In fact, the additional momentum causes the heavier projectile to experience less variation of velocity.

Table 2 compares some dynamic parameters for the pellets at three different Mach numbers. Neglecting the term $(\dot{z}/\dot{x})^2$ of the governing dynamic equations (Eqs. (5) and (6)) gives:

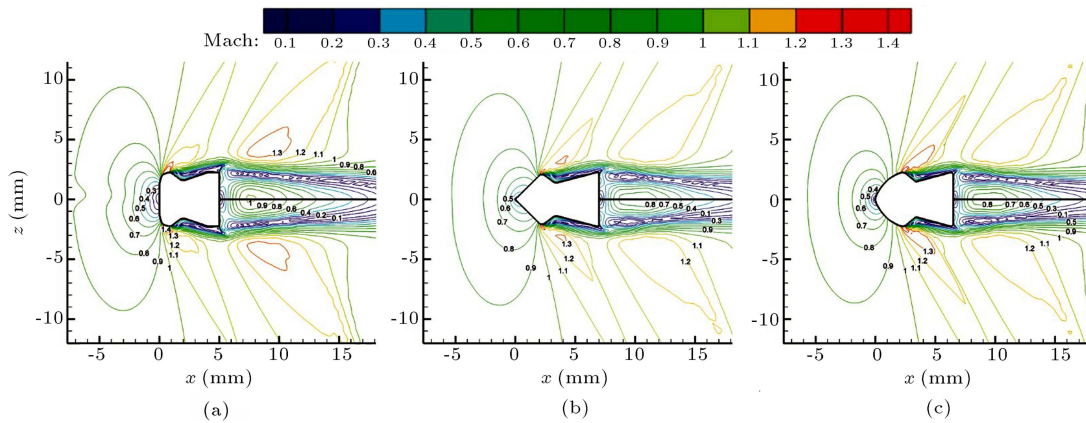


Figure 11. The Mach number contours at $M_\infty = 1.0$ around the (a) 1st pellet, (b) 2nd pellet, and (c) 3rd pellet.

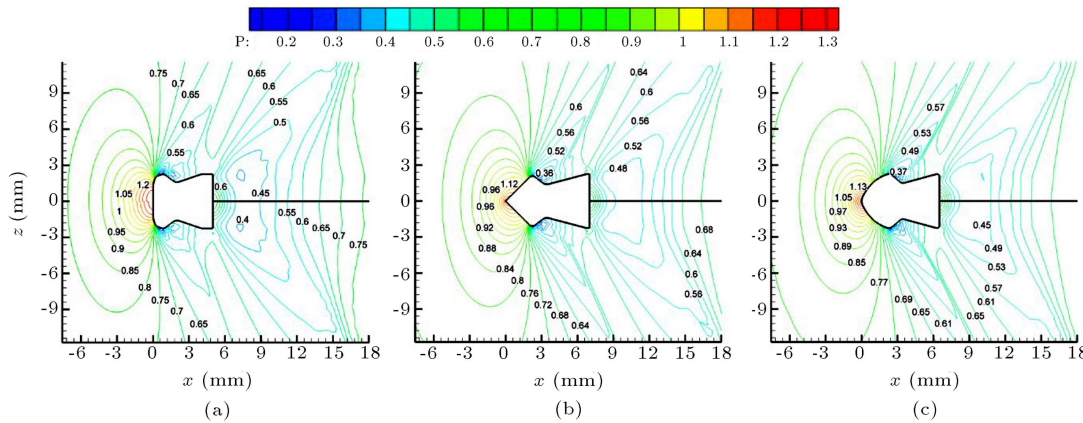


Figure 12. The pressure contours at $M_\infty = 1.0$ around: (a) 1st pellet, (b) 2nd pellet, and (c) 3rd pellet.

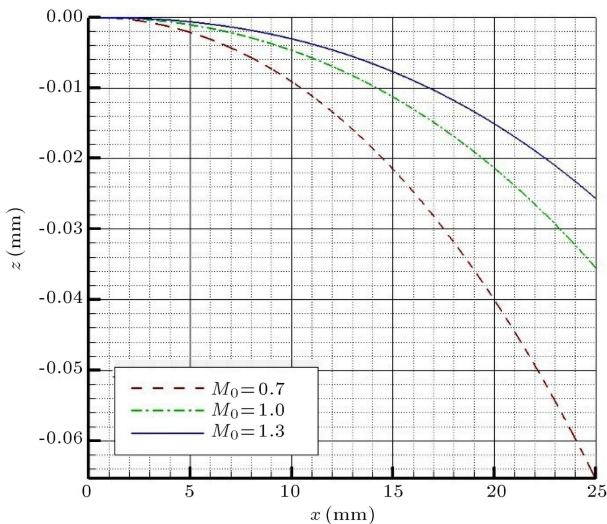


Figure 13. The trajectory of the first pellet at various initial Mach numbers.

$$\begin{cases} \ddot{x} = -\frac{C_D \rho_\infty A_P}{2m} \dot{x}^2 \\ \ddot{z} = -\left(g + \frac{C_D \rho_\infty A_P}{2m} \dot{x} \dot{z}\right) \end{cases} \quad (27)$$

As it is clear, \ddot{x} and \ddot{z} are inversely proportional to the mass of the projectiles. Consequently, if the second

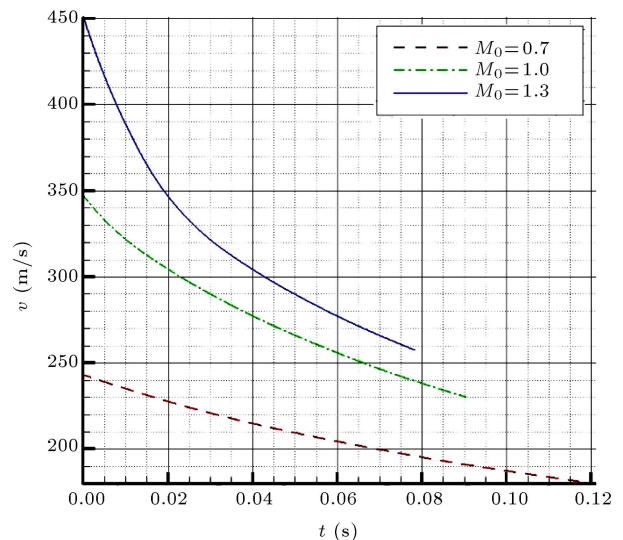


Figure 14. The velocity loss with time in the first 25 m of trajectory for the first pellet.

pellet had had the same weight as that of the other pellets, its altitude change would have been more than that of the third pellet. Hence, the dynamic results for an imaginary pellet of the second type with a mass of 0.5 g have been shown by an asterisk sign (*) in

Table 2. Dynamic results for the first 25 m of trajectory.

Parameter	1st pellet	2nd pellet	3rd pellet	2nd pellet*	M_0
$M_\infty _{x=25}$	0.5174527	0.5363535	0.5309474	0.5105108	
$m\dot{x} _{x=0}$ (kg.m/s)	0.1215160	0.1458193	0.1215160	0.1215160	
$m\dot{x} _{x=25}$ (kg.m/s)	0.0898269	0.1117295	0.0921695	0.0886218	0.7
$t _{x=25}$ (sec)	0.1211390	0.1182580	0.1187510	0.1214850	
$z _{x=25}$ (cm)	-0.0653380	-0.0628998	-0.0632158	-0.0653786	
$M_\infty _{x=25}$	0.6624271	0.7074020	0.7011701	0.6684675	
$m\dot{x} _{x=0}$ (kg.m/s)	0.1735944	0.2083132	0.1735944	0.1735944	
$m\dot{x} _{x=25}$ (kg.m/s)	0.1149936	0.1473612	0.1217192	0.1160422	1.0
$t _{x=25}$ (sec)	0.0905840	0.0872860	0.0879850	0.0901990	
$z _{x=25}$ (cm)	-0.0354590	-0.0335598	-0.0340626	-0.0352461	
$M_\infty _{x=25}$	0.7412338	0.7991596	0.7754770	0.7513526	
$m\dot{x} _{x=0}$ (kg.m/s)	0.2256727	0.2708072	0.2256727	0.2256727	
$m\dot{x} _{x=25}$ (kg.m/s)	0.1286740	0.1664755	0.1346184	0.1304306	1.3
$t _{x=25}$ (sec)	0.0783600	0.0743130	0.0765600	0.0774250	
$z _{x=25}$ (cm)	-0.0256575	-0.0234041	-0.0247747	-0.0250659	

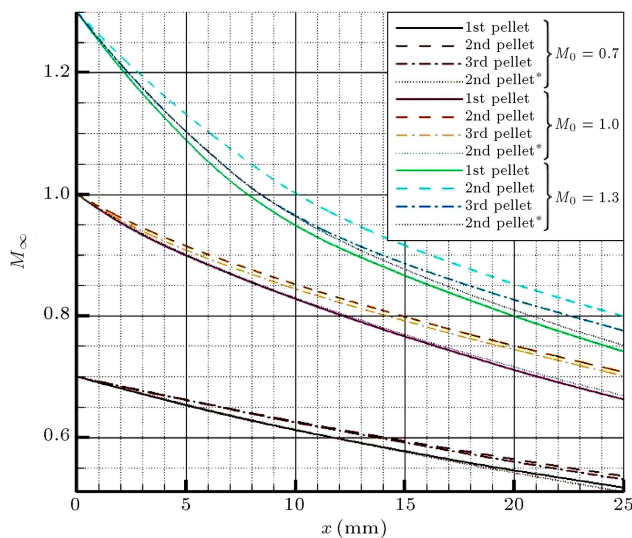
**Figure 15.** The Mach reduction with time for all pellets in the first 25 m of trajectory.

Figure 15 and Table 2, which confirm the foregoing aerodynamic and dynamic analyses.

9. Conclusions

Relying on the aerodynamic analysis, the round-nose pellet (the 3rd pellet) in a variable range of Mach numbers shows the best aerodynamic behavior with respect to the other pellets; however, the 2nd pellet shows the best dynamic behaviors such as altitude loss and final momentum viewpoints. Moreover, the 3rd pellet indicates better dynamic results than the 1st one. In addition, the superior projectile between the

1st and 2nd pellets based on the obtained aerodynamic and dynamic results is the second one. On the other hand, if the second pellet had had the same weight as that of the other pellets (i.e., imaginary second pellet), according to Table 2, the 3rd, 2nd, and 1st pellets would have been preferred, respectively, from aerodynamic and dynamic viewpoints.

References

1. Nietubicz, C.H. and Gibeling, H.J. "Navier-stokes computations for a reacting, M864 base bleed projectile", *Army Research Lab Aberdeen Proving Ground MD*, pp. 1-38 (1995).
2. Silton, S.I. "Navier-stokes computations for a spinning projectile from subsonic to supersonic speeds", *Journal of Spacecraft and Rockets*, **42**(2), pp. 223-230, March-April (2005).
3. Sahu, J. "Parallel computations of unsteady aerodynamics and flight dynamics of projectiles", *Journal of Parallel Computational Fluid Dynamics, Theory and Applications*, pp. 269-276 (2006).
4. Weinacht, P. "Navier-stokes predictions of pitch damping for axisymmetric projectiles", *Journal of Spacecraft and Rocket*, **34**(6), pp. 753-761 (1997).
5. Silton, S.I. and Weinacht, P. *Effect of Rifling Grooves on the Performance of Small-Caliber Ammunition*, 23rd International Symposium on Ballistics, pp. 775-782 (2007).
6. DeSpirito, J., Silton, S.I. and Weinacht, P. "Navier-stokes predictions of dynamic stability derivatives: Evaluation of steady state methods", *AIAA-2008-0214*, Jan (2008).

7. Sahu, J., *Virtual Fly-Out Simulations of a Spinning Projectile from Subsonic to Supersonic Speeds*, 29th AIAA Applied Aerodynamics Conference, Honolulu, Hawaii, June (2011).
8. Sahu, J., Heavey, K.R. “Parallel CFD computations of projectile aerodynamics with a flow control mechanism”, *Computers & Fluids*, **88**, pp. 678-687, December (2013).
9. Kumar, A., Panda, H.S., Biswal, T.K. and Appavuraj, R. “Flow around a conical nose with rounded tail projectile for subsonic, transonic, and supersonic flow regimes: A numerical study”, *Science Journal*, **64**(6), pp. 509-516, November (2014).
10. Jameson, A. “Iterative solution of transonic flows over airfoils and wings, including flows at Mach 1”, *Pure Appl. Math*, **27**, pp. 283-309 (1974).
11. Jameson, A. “Full potential, and Navier-Stokes schemes”, *Applied Computational Aerodynamics*, Edited by P.A. Henne, *Progress in Astronautics on Aeronautics*, **125**, pp. 39-88 (1990).
12. Jameson, A. “Positive schemes and shock modeling for compressible flows”, *International Journal for Numerical Methods*, **20**, pp. 743-776 (1995).
13. Smits, A.J. and Dussauge, J.P. *Turbulent Shear Layers in Supersonic Flow*, Birkhäuser, ISBN 0-387-26140-0, p. 46 (2006).
14. Zhao, Y. and Murali, D. “Multigrid computation of flow past airfoil using K- ϵ turbulence model”, *Journal of Aerospace Engineering*, pp. 180-188, October (1995).
15. Swanson, R.C., Turkel, E. and White, J.A. “An effective multigrid method for high-speed flows”, *Communications in Applied Numerical Methods*, **8**, pp. 671-181 (1992).
16. Tan, D. and Chen, Z. “On a general formula of fourth order Runge-Kutta method”, *Journal of Mathematical Science & Mathematics Education*, **7**(2), pp. 1-10 (2012).
17. Pasandideh Fard, M. and Srinivas, K. *An Investigation of Renormalization Group Based Algebraic Turbulence Model*, Twelfth Australasian Fluid Mechanics Conference, the University of Sydney, Australia (1995).
18. Lin, H. and Chieng, C.C. “Aerodynamic computations for a transonic projectile at angle of attack by total variation diminution schemes”, *Journal of Spacecraft and Rockets*, **30**(3), pp. 304-315 (1993).

Biographies

Mehdi Rafeie received his BSc degree in Mechanical Engineering from Azad University of Mashhad, Iran, in 2006, and his MSc degree in Energy Conversion from Ferdowsi University of Mashhad, Iran, in 2009. He has already published two papers in international conferences. Currently, he is a PhD student at the University of New South Wales, Sydney, Australia.

Ali Reza Teymourtash received his BSc degree in Mechanical Engineering from Ferdowsi University of Mashhad, Iran, in 1983, and his MSc degree in Mechanical Engineering (thermo fluids) from Sharif University of Technology, Tehran, Iran, in 1987, and his PhD degree in Energy Conversion from Ferdowsi University of Mashhad, Iran, in 2002, where he is now Associate Professor. He has published a book in Fluid Mechanics, 40 papers in respected international conference proceedings, and 28 journal papers. He has also been responsible for a number of applied projects.